The Implementation of Influence Boundary Procedures in CFD

Kehinde Alabi[*] and Foluso Ladeinde.[†]

Thaerocomp Technical Corp., P. O. Box 1527, Stony Brook, NY, 11790-0609

The current paper presents and categorizes influence boundary methods. These are computational fluid dynamics procedures that are based on reducing the scope and resource requirement of a computational fluid dynamics problem while minimizing the error in the approximated domain by a systematic application of the effect of the full or surrounding domain on the reduced one. The objective is to present a useful tool for computationally-intensive CFD applications. Equations and automatic procedures for determining the reduced domain are presented. The procedure is validated using flow over a cylinder, airfoil, and the B747-200 aircraft. The error in the procedure is determined for an airfoil/flap and wing/store configuration. The results show that the automatically-determined influence domain procedure, aside from obviating the need for ad-hoc determination of the size and shape of the influence domain, it also minimizes the error in the influence boundary calculation. In addition, it is demonstrated that calculations with errors below 20% at *Ma* = 0.25 and 10% at *Ma* = 0.8 can be performed at about 30% of the computational cost of a full domain calculation.

Nomenclature

α_w	=	wing or airfoil angle of attack
α_f	=	flap angle of attack
C_p	=	pressure coefficient
C_L	=	lift coefficient
C_D	=	drag coefficient
C	=	airfoil or wing chord length
F_i	=	influence boundary determination function
L_{ref}	=	reference length
M_∞	=	free stream Mach number
P	=	pressure
u, v, w	=	velocity components in the *x, y, z* Cartesian coordinate directions, respectively
w_i	=	influence boundary function weight

I.   Introduction

Many realistic aerospace systems, such as those involving moving body parts and/or large complicated aerospace vehicles, store release from aircrafts, aircraft in vertical take-off/landing or in ground effect, booster rocket separation, etc., are still very expensive to simulate. Influence boundary methods take advantage of possible simplifications in the geometry or physics in order to obtain significant reduction in the time or resources required to perform such simulations.[1,2]

Influence boundary methods are still in the early stages of development and general, automatic procedures to identify their occurrence and decompose a CFD domain on the basis of influence boundaries have not received enough attention. In addition, studies are required to formulate and test boundary treatments across influence domains at different relative simulation times and/or involving relative motion.

---

[*] Research Engineer, Ph.D, AIAA Member.
[†] Director of Research, AIAA Life Member & Associate Fellow.

A. Types of Influence Boundary Problems

The following types of influence boundary problems can be identified:

(1) Unsteady problems in which only a small portion of the flow field is unsteady. An example is aircraft/store separation problem, Fig. 1. The entire flow field could be decomposed into a region surrounding the unsteady parts and a region where flow is essentially steady. This will lead to substantial savings in the overall cost of simulation. Using a similar strategy, Davis et. al.[1] observed savings of 4-8 orders, without significant loss in the accuracy of the simulations.
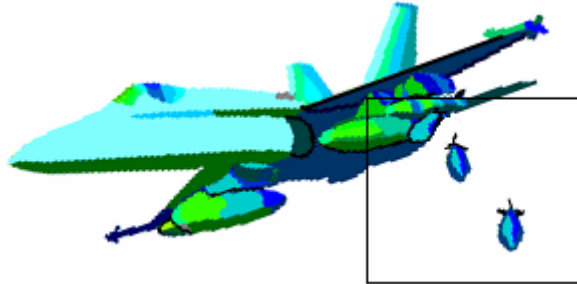
Figure 1. JDAM Store Separation from an F/A-18CD Aircraft.

(2) Steady state problems to which simplified physical models can be applied to most parts of the flow field. For example, many high-speed aerospace calculations involve a viscous, near-wall region where the full Navier-Stokes equations must be solved, and surrounding regions where the Euler equations might be sufficient. Substantial savings will accrue from this kind of physics-based partition, compared to solving the entire domain with a viscous Navier-Stokes model.

(3) Problems in which only a small (minimized) portion of the flow field may be analyzed. The effect of the surrounding or remaining portion of the flow field may be approximated and applied to the minimized domain. An example is a simulation of a complete aircraft. A calculation of this type may take several weeks to complete.[3,4] In adding a new feature such as a store or other payload to the airplane, the entire configuration has to be recalculated. A procedure that allows very good estimates or results to be obtained based solely on simulation of the new feature and approximating the effect of the entire previously computed aircraft will offer significant savings to a design process.

(4) Combination of (1), (2) and/or (3), or the presence of isolated unsteady regions, as well as regions with different physics, and/or calculations based only on a minimal portion of a large CFD domain.

The development and implementation of an influence boundary CFD capability involve the following tasks:
1. Automatic identification of influence boundary problems. Most influence boundary calculations are currently identified and set up manually[1] as no general and/or automatic procedures exist to facilitate the identification of the boundaries for a variety of problems.
2. Automatic decomposition of a flow field into separate, contiguous influence domains.
3. General and robust application of various boundary conditions on influence boundary sub-domains, including those with moving boundaries.

The first part of this paper investigates the decomposition of a flow field into influence domains. The task involves trimming overlapping domains along influence boundary lines and subsequent solution of the appropriate flow equations in the domains.

The second part of this paper focuses on the feasibility of performing influence boundary calculations of type (3). Influence boundary calculations based on manually defined domains of different sizes are performed and the results are compared with calculations in which the influence boundary domain is determined automatically. The errors in the influence boundary simulations are calculated and the results analyzed.

The current implementation utilizes the overset (Chimera) procedure to connect the component grids and the CFD General Notation Scheme (CGNS) to coordinate CFD data exchange between the various calculations and solvers. The details of the procedure as well as the formulation of the automatic influence boundary determination procedure are presented in the next section.

B. The Overset Method

The overset or Chimera method[3-9] is a computational tool that enables the generation of grids over a complicated domain using separate sub-domains that are joined together by interpolation during the solution phase. This method has facilitated the CFD calculations of flow over complete aircraft and other complicated geometries.[7-8,10]

The overset procedure of removing redundant grid points in overlapping meshes that duplicate sections of the computational domain is referred to as "hole-cutting" when the area removed approximates solid objects or "optimizing" when the area is removed because another mesh better approximates; or is expected to better approximate; the region. Noack[11] provided a review of the procedures used to achieve an optimum domain from an assembly of overlapping grids. Some of these are summarized below.

Analytic Shapes
This method uses analytic shapes, or cookie-cutters, to trim sections of the domain to form an optimum domain. This requires a lot of user input for all but the simplest geometries. Such user controlled procedures are sometimes referred to as manual hole-cutting or blanking methods.

Point Normal Comparison
This method applies user defined grid surfaces as cutters or boundaries for other grids. The dot product of the surface normal and a vector from the surface to a point on other grids is used to decide whether or not the point lies inside the surface. This method also requires a lot of user input.

Stencil Search
This method examines every grid point and searches for potential donors. If a donor is not found, the point is marked as a hole point. This algorithm may fail for bodies that are not completely enclosed.

Octree Based Data Structures
The octree (3D) and quadtree (2D) procedures are memory-efficient ways to discretise a domain using small Cartesian recursive subdivisions. When the size of a unit of the tree is small enough to approximate the solid boundaries, the tree data can be used to quickly locate points in the domain. The location of the point can then be used to determine whether or not the point lies within a cutting surface. The cutting surface in this procedure is usually taken to be the geometric boundary determined from the problem description data. Procedures requiring no extra user input to perform the hole-cut process are referred to as automatic hole-cutting methods.

Optimization Functions
Optimization functions are used to trim grids that excessively overlap. Regions of excessive overlap can be identified as parts of the computational domain where more than one cell from different blocks approximate the same location and none of them has overset nodes. The donor suitability function (DSF) introduced by Noack[11] defines a scalar at each location in the overlap region. The cell with the best value of this function is the preferred cell. All other cells approximating the same location are removed since they are redundant. The DSF chooses this scalar as the largest edge size of the cell thus ensuring that the most refined mesh is retained over more coarse meshes.

It should be noted that the choice of overset and donor nodes can have significant effects on the overall accuracy of the solutions.[11] The methods listed above use geometric factors for selecting the optimum combination of overset/donor nodes. We propose that fluid dynamical issues such as the flow direction, and the presence or absence of shock waves and boundary or shear layers, should also be considered in generating the overset/donor combinations. This is the approach used in the present work. It should be noted that for moving boundary problems, the introduction of the procedure described in the present paper does not introduce significant increase in the hole-cut and optimization process since this step is already performed at every time step.

II. Formulation

The development of an influence boundary model is described in this section.

A. Identification of Influence Boundary Limits

For the current work, given a set of overlapping grids approximating the computational domain, a set of equations is devised to trim and optimize the computational domain along influence boundary lines. This equation will take the following functional form:

$$F_T = w_1 F_1 + w_2 F_2 + w_3 F_3 + \ldots, \tag{1}$$

where the F_is are functions related to an influence boundary criterion, and w_is are weights for each criterion. Several criteria are used to determine the location of influence boundaries in the current work. These strategies are based on the following principles:

1. Separation along lines of flow physics

To detect a high gradient region, such as a shear or boundary layer (i.e. in the vicinity of a solid wall), the form of the function F could be based on the gradient of the velocity field, local Reynolds number, or ratio of the local velocity u to the free stream velocity, U_F, at that location:

$$F_1 = \frac{1}{1 + \max[|\partial u / \partial x_i|]}, \tag{2}$$

where i are the axes directions in the computational coordinate system. Note that $F_1 \rightarrow 1$ in the far field (inviscid region).

To detect unsteadiness, we examine the solution variables as a function time.

$$F_2 = \frac{1}{1 + \max[|\partial \phi / \partial t|]}, \tag{3}$$

where $\bar{\phi} = [\rho, u, P, \ldots]$ and $F_2 \rightarrow 1$ for steady state grids.

Influence boundaries could also be determined on the basis of the existence of strong gradients, such as discontinuities, shock waves, etc. In the current work, in order to contain shock waves within the domains, we have used a function of the form

$$F_3 = \frac{1}{1 + \max[|\partial P / \partial x_i|]} \ . \tag{4}$$

2. Selection of better solutions

This factor pertains to the overset donor search process, where an overset node has several possible donors from different overlapping grids. Previous work[11,12] has considered geometric factors such as the selection of blocks containing cell sizes that are closest to those of the recipients. For example, the PEGASUS code defines a cell difference parameter for this purpose.[12] In addition to the foregoing criteria, the current work also preferentially considers cells from upwind grids. Also, boundary or shear layer grids are preferred to free-stream grids.

3. Geometric

This is the traditional geometric criterion used in optimizing grids. PEGASUS[12] uses an "overlap optimization" algorithm that is based on matching grid sizes as closely as possible. Nakahashi[13] uses an algorithm that seeks to place the boundary at the minimum possible distance from solid walls. The donor suitability function introduced by Noack[11] defines a scalar at each grid point that determines the preferred cell at an overlap point. This approach is adopted in the present work. The geometric factor is incorporated via the function F_4, defined as

$$F_4 = \frac{1}{1 + \max[\,{}^1\!/\!_{\Delta x_i}\,]}, \tag{5}$$

where i are the axes directions in the computational coordinate system.

III.   Results

The influence boundary procedure described in the previous sections was implemented in the AEROFLO[14] multidisciplinary solver, developed by Thaerocomp Technical Corp. Results and validation procedures are presented in this section. Validation calculations are for flow over a cylinder, airfoil, and B747 aircraft. These calculations also demonstrate the feasibility of influence boundary calculations of Type (2). Results are also presented for influence boundary calculations of Type (3) for flow over an airfoil/flap and wing/store calculations. The calculations are designed to demonstrate that the influence boundary determination equations optimize the influence boundaries while minimizing the errors in the calculations. It should be noted that while the influence boundary procedure described in this paper has been implemented for structured overset grids, the procedure can also be easily implemented for unstructured grids.

A. Validation of Influence Boundary Calculations

Validation of the formulation for automatically determining the influence boundary domain in Eq. (1) were done using influence boundary calculations of type (2) or calculations solving less detailed equations in parts of the flow field resulting in computational savings with little or no loss in accuracy. The flow over a cylinder, airfoil, and B747 aircraft are computed using the complete Navier-Stokes equations and the results compared with calculations in which the complete Navier-Stokes equations are solved in a minimized domain while the Euler equations are solved everywhere else. The results are presented in this section.

1. Flow over a Circular Cylinder

The flow past a circular cylinder at $M_\infty = 0.1$ and $Re = 100$ was calculated. The model consisted of two overset grids shown in Fig. 2. The first grid, "A", contains a body-fitted mesh around the cylinder with the mesh concentrated around the surface due to the viscous layer expected around the solid. The second grid is a coarser grid extending far-field, or about 40 times the diameter of the cylinder. This grid was preferentially cut by the first grid using the overset procedure. The near-wall grid contains 257 x 101 points, while the far-field grid contains 128 x 128 grid points. Three sets of calculations were performed. The first calculation solved the Navier-Stokes equations in both grids while the calculation solved the Navier-Stokes equations in the near-wall grid and the Euler equations in the far-field grid. For the third calculation, the procedures described in this paper were used to obtain two influence boundary grids which were then solved as in the second case. In all cases, the Navier-Stokes equations were solved with a sixth-order compact scheme for spatial differencing with compact filters.[15] The Euler equations were solved with a second-order central differencing scheme. Fourth-order Runge-Kutta procedure was used for time integration.
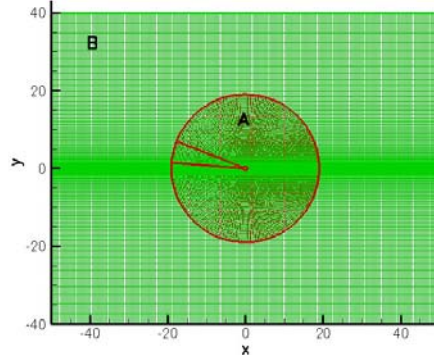
Figure 2. Mesh used for the calculation of flow past a cylinder.

Figure 3 illustrates the effects of using the influence boundary equations presented earlier in this paper. Fig. 3(a) is the overset grid set when the inner grid is selected as the preferential grid. Fig. 3(b) shows the grid assembly when only the geometric factor (Eq. 4) is used as the boundary determination criterion. Fig. 3(c) shows the grid assembly when the velocity gradient (Eq. 2) is used as the boundary determination criterion. The domain defined by the inner grid is then expected to be the region in which viscous conditions prevail. Finally, Fig. 3(d) shows the boundaries when the combined influence boundary decomposition criteria are applied (Eq. 1).

a)

b)

c)

d)
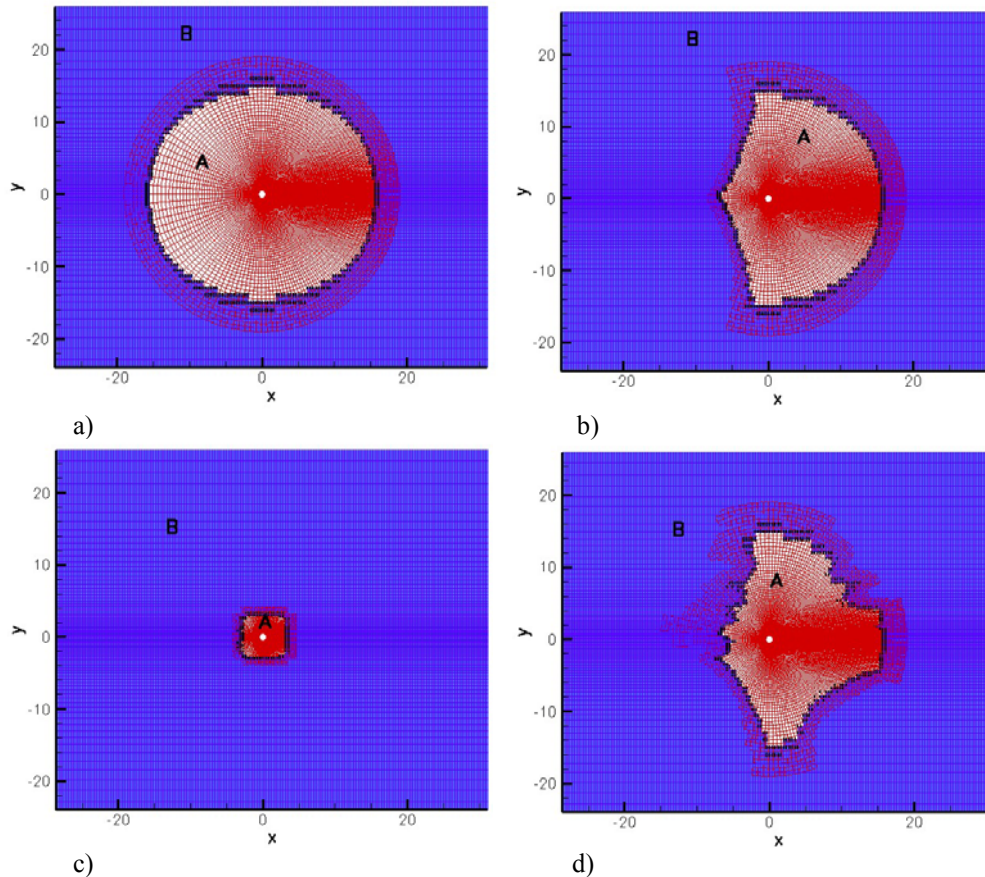
Figure 3. Influence boundary grids obtained using different criteria: (a) viscous grid is selected as the preferred grid, (b) geometric factors determine the preferred grid, (c) gradient of velocities, (d) combined factors criteria (Eq. 1). The overset nodes at the border between the two grids are indicated.

Figure 4 shows the vorticity contours around the cylinder for all three calculations. All calculations preserve the vortex shedding profile. Fig. 5 shows the C_p profile around the cylinder for all three calculations. No significant differences are evident. The total CPU times in seconds required for the calculations are shown in Table 1. A gain of

about 1.5 times can be observed in using the influence boundary procedure relative to the solution of the full Navier-Stokes calculation in both grids.

(a)   (b)
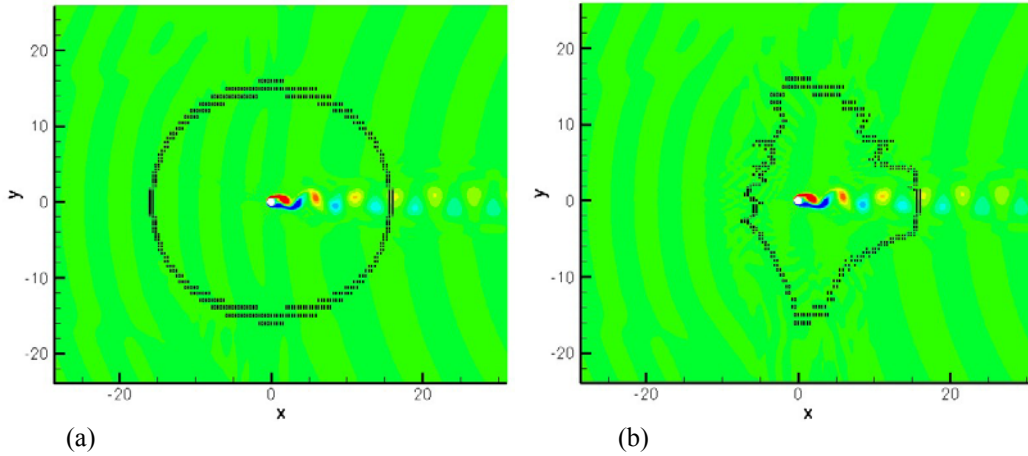
Figure 4. Vorticity field showing the shed vortices from the cylinder for (a) viscous grid is selected as the preferred grid and the complete Navier-Stokes equations are solved in both grids, (b) Equation 1 is used to determine the boundary between the grids, and Euler equations are solved in the far-field grid and Navier Stokes equations in the near-wall grid. The overset nodes at the border between both grids are indicated.
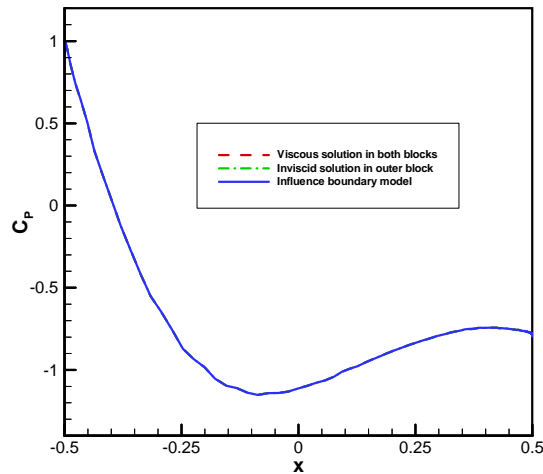
Figure 5. Coefficient of Pressure C_p profile around the cylinder.

Table 1. CPU Time Taken by Calculations of Flow Past Cylinder

Procedure	CPU Time (seconds)
Viscous calculations in both blocks	3105101.692
Inviscid calculations in outer block, viscous in inner	2314821.4826
Influence boundary model	2045122.4187

2. Flow over an RAE2822 Airfoil

The influence boundary procedure was also used to investigate flow around an RAE2822 airfoil at $M_\infty = 0.75$ and an angle of attack, $\alpha = 2.31^o$, $Re = 6.5 \times 10^6$. An overset grid system consisting of two blocks was used for the calculation. The first grid contained a body-fitted grid around the airfoil with dense elements close to the solid body, while the second grid is a coarse grid with boundaries extending over a region around the airfoil where the

assumption of free stream conditions is expected to be valid. Each grid contains 157 x 50 grid points. A hole-cut was performed such that the inner grid contained the solution within the vicinity of the airfoil, while the outer grid was cut in this same region. Instantaneous flow results are exchanged between the grids at every time step.

Two sets of calculations were performed. The first calculation solved the Navier-Stokes equations in both grids with the relative boundary between the two grids determined by the inner grid. The second calculation solved the Navier-Stokes equations in the inner grid and the Euler equation in the outer grid, whereby the influence boundary equations were used to dynamically determine the boundaries between the two grids (Eq. 1). The Navier-Stokes equations were solved with a fifth-order WENO[16] scheme, the Euler equations were solved with the second-order MUSCL scheme. Fourth-order Runge-Kutta procedure was used for time integration.

a)   b)
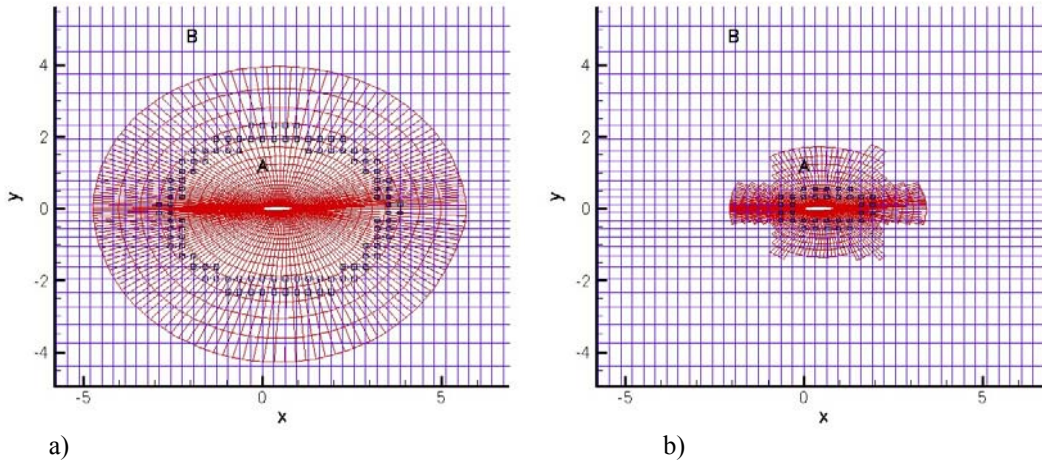
Figure 6. Influence boundary grids obtained using different criteria: (a) the viscous grid is preferred grid, (b) influence boundaries determined using the combined factors in Eq. (1). The overset nodes at the border between both grids are indicated.

Figure 6 shows the two grids, while Fig. 7 presents the coefficient of pressure around the airfoil. Agreement between the influence and non-influence boundary model is evident. The influence boundary calculations required about 55% of the CPU time for a full domain calculation.
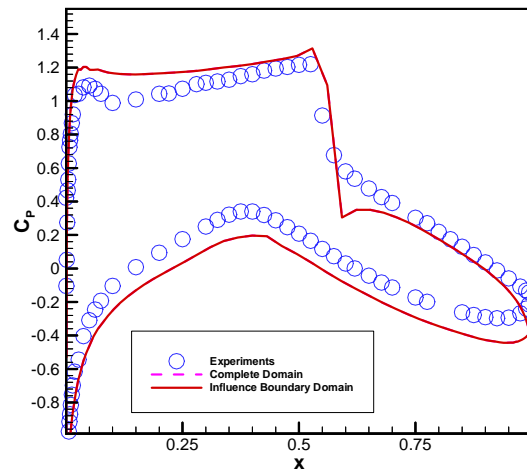
Figure 7. Coefficient of Pressure C_p profile around the airfoil.

3. Influence Boundary Model for the Boeing B747-200 Aircraft

The reference grid for the Boeing 747-200 aircraft investigation of influence boundary models is shown in Figs. 8 and 9. The base grid, Fig. 8(a), consists of six grids extending from the body of the aircraft to about 30 times the wing chord length. A close up of the grid close to the body of the plane is shown in Fig. 8(b). For the influence boundary studies, the base grid was modified to include a far-stream grid, as illustrated in Fig. 9(b). The boundary between the grids was determined using Eqs. (1) and (5). In both calculations, the extent of the total computational domain is about 30 times the chord length, as evident from Fig. 9(b).

The base calculation on the grid shown in Fig. 9(a) is the complete Navier-Stokes equation. For the influence boundary model, the Euler equations were solved in the far-field, while the Navier Stokes equations were solved in the near-wall grids. The WENO scheme was used for both calculations with Beam-Warming scheme for time integration. Details of the full domain calculations as well as difficulties encountered are presented in a different paper.[17] The pressure contour on the surface of the airplane is presented in figure 10. Figure 11 shows a comparison of the coefficient of pressure, C_p, at selected sections along the aircraft wing. The results show close agreement between the full domain, complete Navier-Stokes calculations and the minimized domain Navier-Stokes/Euler calculations. The influence boundary calculations required about 84% of the CPU time for a full domain calculation.

a)   b)
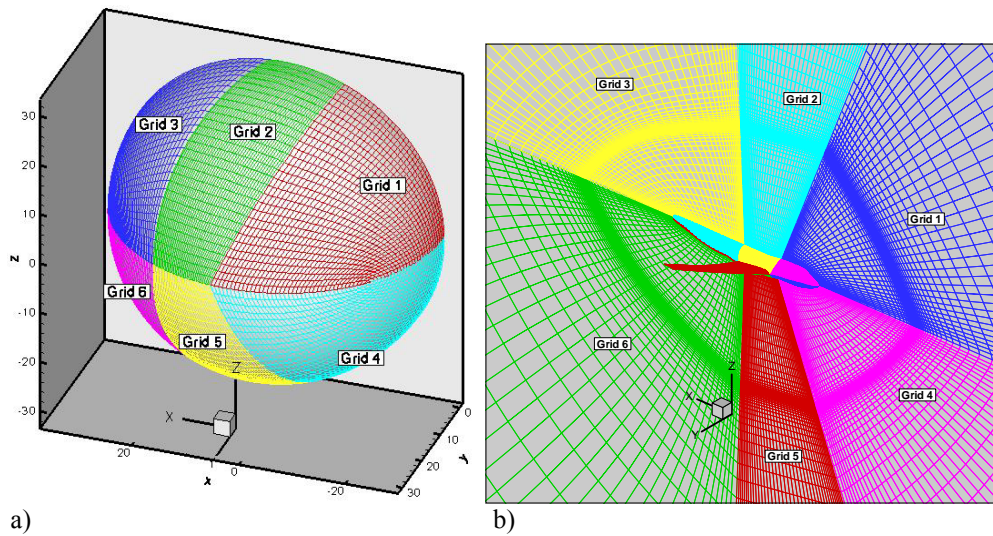
Figure 8. Mesh used for the initial computation of flow around the B747.

a)   b)
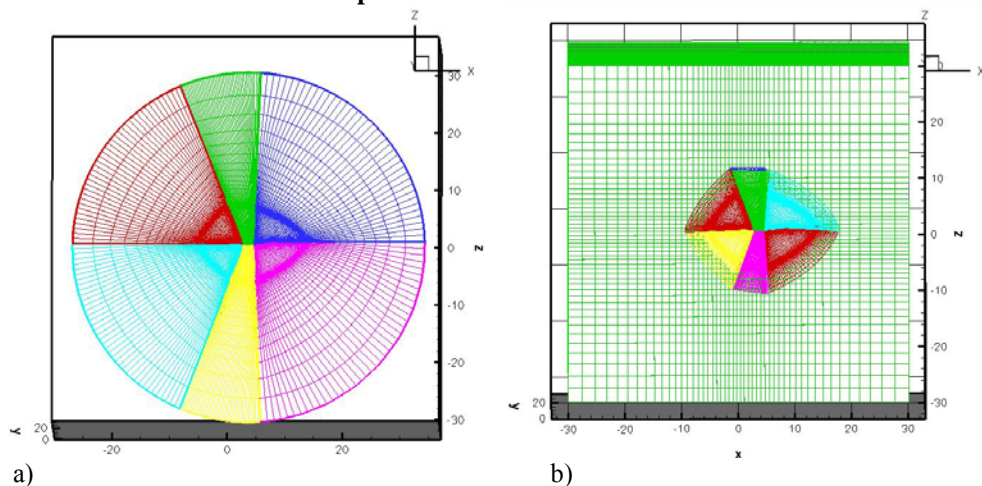
Figure 9. (a) Original grids, (b) Grids with far-field grid with boundary determined by Eqs. (1) and (5).
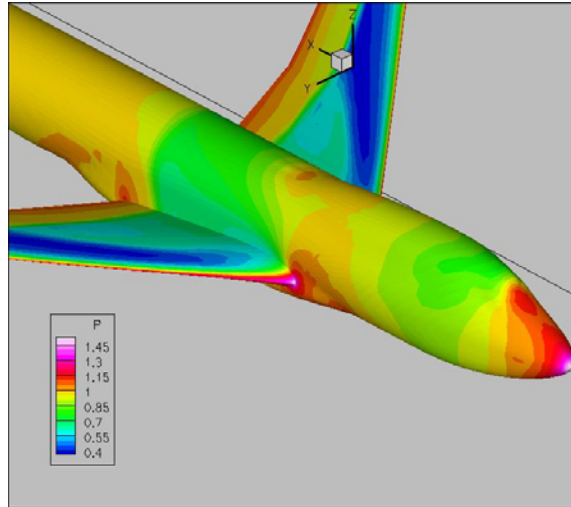
Figure 10. Pressure field around the B747-200 aircraft.
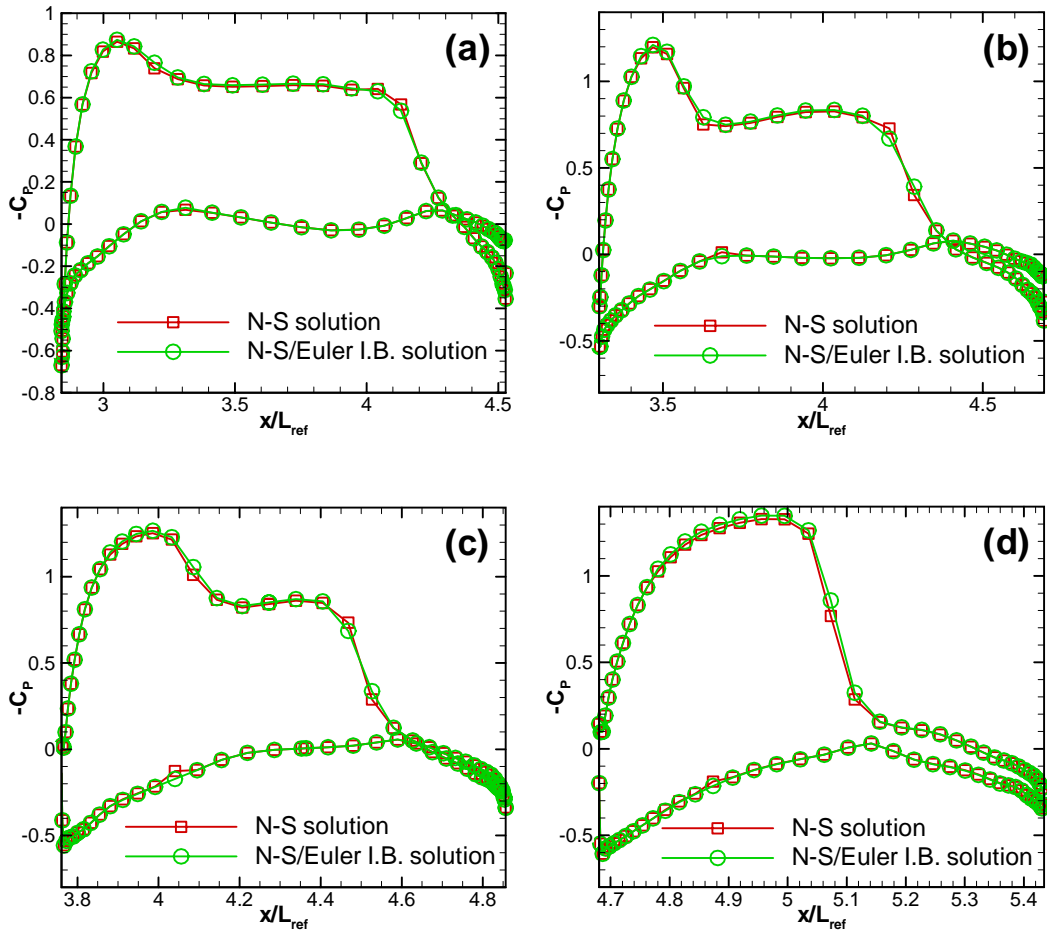
Figure 11. Coefficient of pressure, C_p, at y/L_{ref} = (a) 0.5, (b) 1.0, (c) 1.5, and (d) 2.5.

B. Influence Boundary Calculations of Type (3)

Calculations of this type are demonstrated with the wing/store and airfoil/flap configurations. In both cases, influence boundary calculations are performed in a minimized domain focusing on a small region around the store or flap and approximating the effect of the surrounding wing or airfoil through boundary conditions. These calculations are compared with those based on a complete calculation of both wing and store or airfoil and flap. The results are discussed in this section.

1. Airfoil/Flap Configuration

Calculations were done for flow past an airfoil/flap combination. The physical domain is illustrated in figure 12. The dimensions in the figure are in inches. The airfoil has a NLR(1)-0015 profile while the flap has a NACA 64(1)-112 profile. The model is two-dimensional. The objective of the calculations is to validate the influence boundary equations presented in section 2 as well as to estimate the error in the influence boundary calculations of type (3). Calculations were done at Mach number, $M_\infty = 0.25$ and 0.8, two angles of attack, $\alpha_w = 0^o$ and 5°, and four flap angles, $\alpha_f = 0^o$, 10°, 20°, and 30°. The calculations are based on the Euler equations. For spatial differentiation the compact scheme is used for the lower Mach number and the WENO scheme for the higher Mach number. The Beam-Warming scheme is used for time integration. The airfoil chord length, C, was used as the length scale.
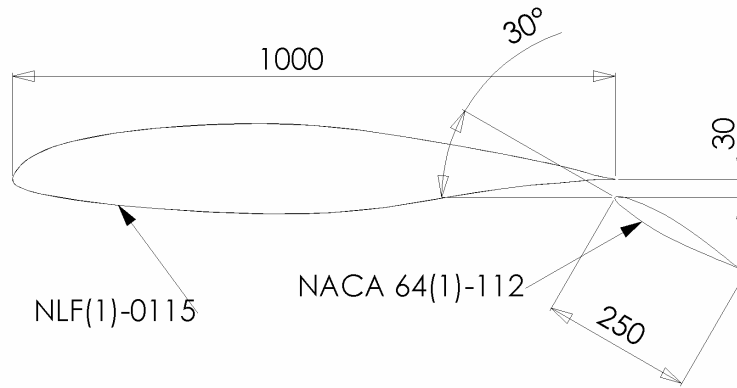
Figure 12. Airfoil/Flap Configuration.
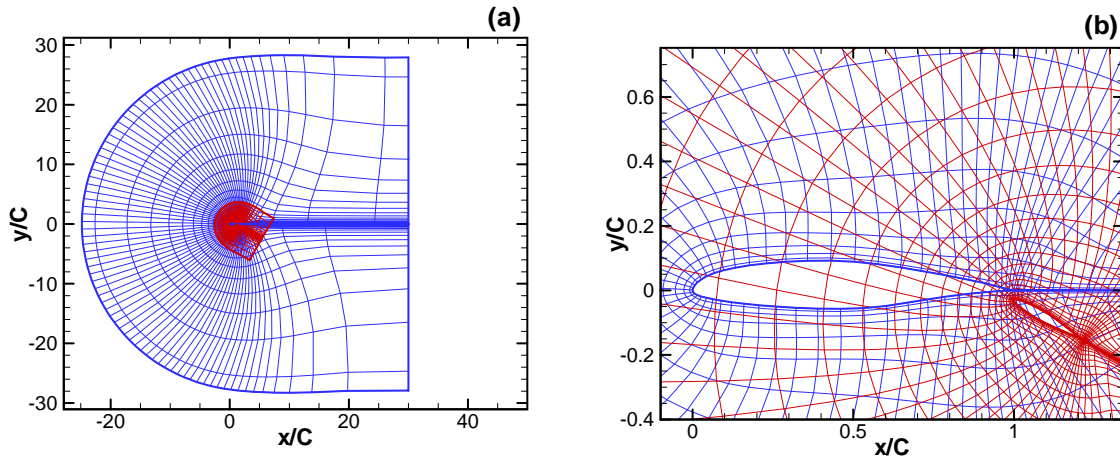
Figure 13. Grids at 30° flap angles after rigid transformations (a) Airfoil and flap grid after scaling and rotation, (b) Close up view.

The airfoil and flap grids were generated separately and are shown in figure 13. The grids were assembled as a pre-processing step transforming appropriately for the different flap angles and position. Following the transformation, hole cuts were made between both grids using the overset procedures and calculations were

performed to obtain the results for the full domain (airfoil and flap). The grids following the overset assembly is shown in figure 14.

Two types of calculations are performed. In the first type, the flow over the integrated airfoil and flap configuration is calculated. In the second type of calculation, or influence boundary calculations, flow over the store alone is calculated using a small grid surrounding the store. Boundary conditions to this calculation are provided using values from calculations of the airfoil alone. The differences between both types of calculations are computed.

The influence boundary calculations used three minimized domains of different sizes as well as one minimized domain using the procedure described in section 2. The three influence boundary domains are shown in figure 15.
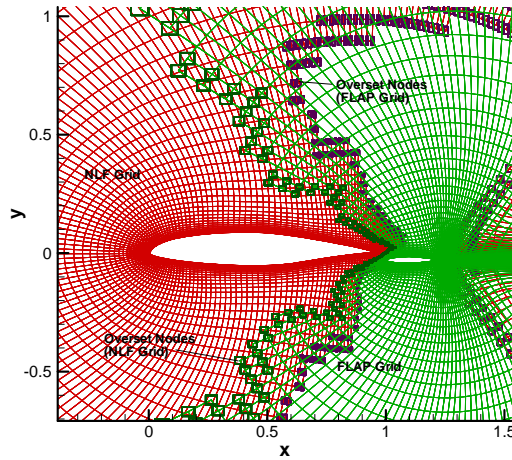
Figure 14. Overset grids following hole cut. Notice the number of fringe nodes and between the grids required to perform high-order interpolation between the grids.
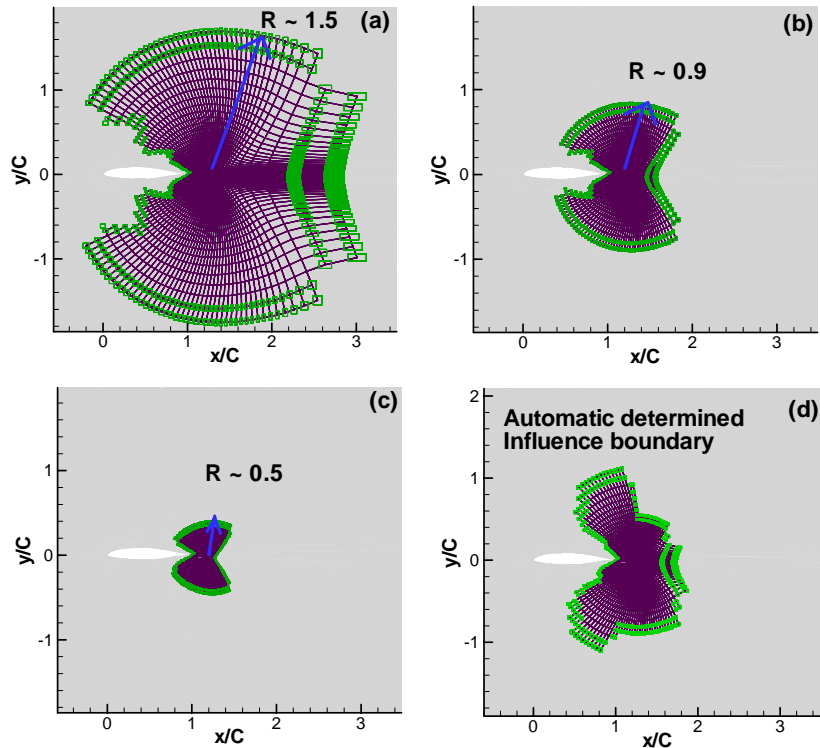
Figure 15. Influence boundary grids: (a) Domain 1, (b) Domain 2, (c) Domain 3, (d) Automatically generated influence domain.

12
American Institute of Aeronautics and Astronautics

1.1 Convergence Studies

To determine convergence of the calculations, the residuals of the calculations were monitored as well as the plots of the results in time. For the coarse calculations, the residual and the coefficient of pressure, C_p results at separate time intervals are shown in Fig. 16.
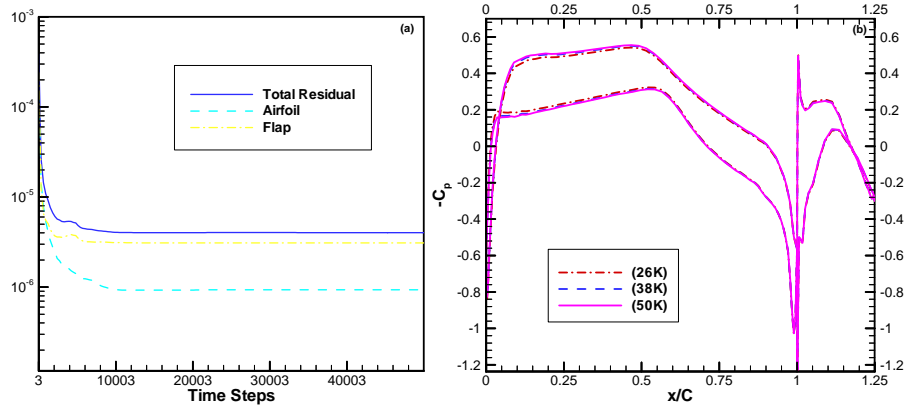
Figure 16. Calculations at different time intervals showing convergence to a single solution for the coarse grids (a) Error norm of the calculations, (b) C_p at the surface of the airfoils.

1.2 Grid Sensitivity Studies

Grid sensitivity studies were done using three different grid sizes shown in the table below.

Table 2. Grid Sizes used for the Airfoil/Flap Calculations

Grids	Coarse	Medium	Fine
Airfoil	201 x 53	251 x 68	301 x 82
Flap	81 x 42	121 x 53	141 x 62

The results of the sensitivity calculations for the three grids are shown in Fig. 17 for the coefficient of pressure. Based on the results, the intermediate or medium grid was chosen for all subsequent calculations.
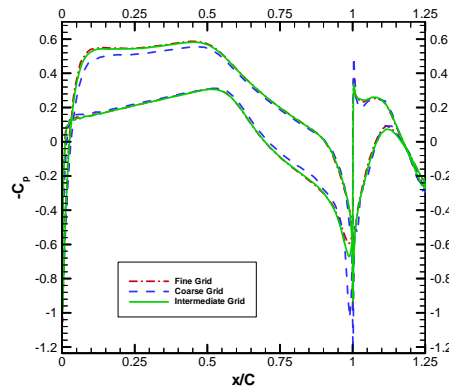
Figure 17. Comparison of C_p for the different grids after the solution in each grid has converged.

1.3 Calculations of Airfoil Only

Figure 18 shows the coefficient of pressure, C_p for the wing only at 0° and 5° angles of attack and Mach number, M_∞ = 0.25 and 0.8. These two calculations were used as basis for the influence boundary calculations.

American Institute of Aeronautics and Astronautics
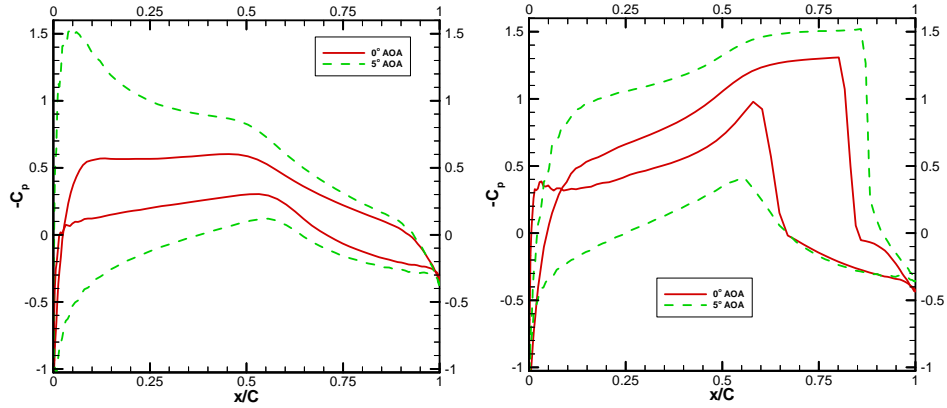
Figure 18. Coefficient of Pressure, C_p, for NLF(1)-0115 wing alone at 0° and 5° angles of attack (a) $M_\infty = 0.25$, (b) $Ma = 0.80$.

1.4 Full Domain Calculations

Figure 19 shows the full domain calculations for the wing and flap at 0° and 5° angles of attack and Mach number, $M_\infty = 0.25$ and 0.8. The results show that the flap angle has a significant effect on the wing solution. This effect will not be captured by influence boundary calculations that perform calculations on the flap alone without any feedback to the wing. Therefore, the influence boundary calculations are expected to include inherent errors. An objective of the current study is to minimize this error.
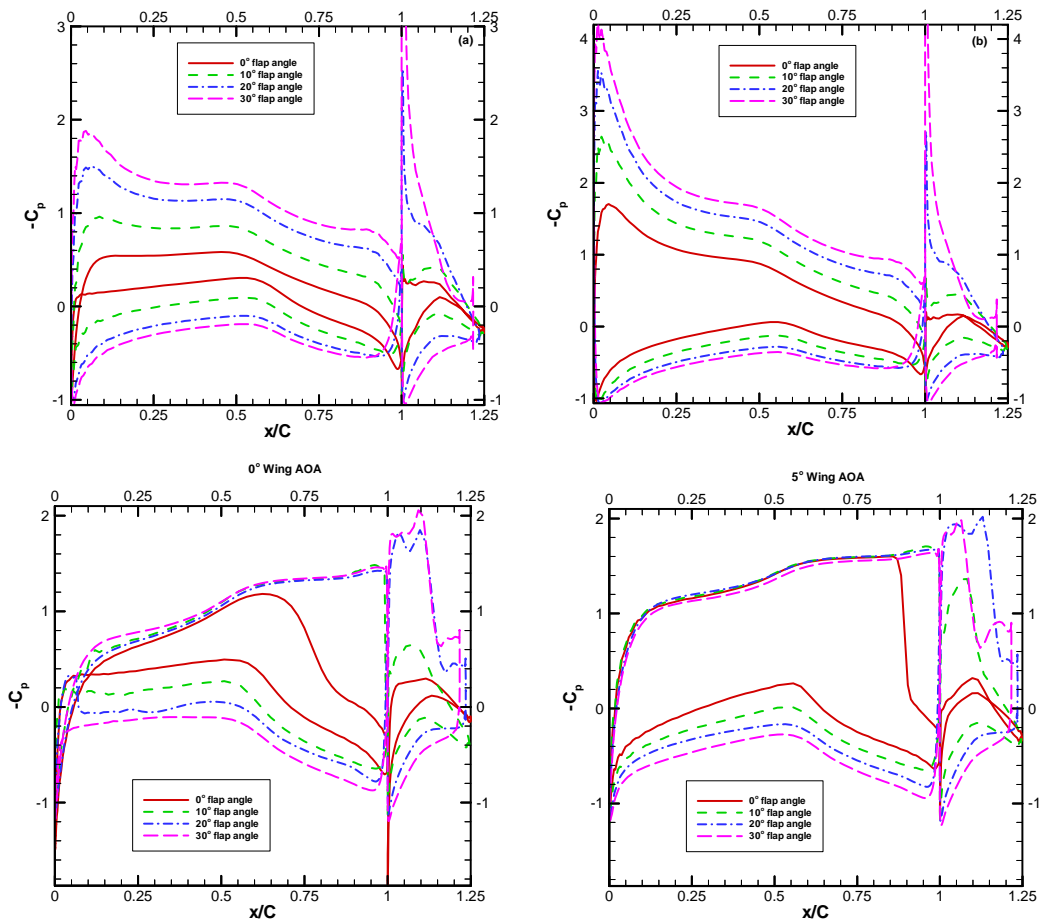
Figure 19. Coefficient of pressure, C_p, for the wing-flap calculations showing the effect of Mach number and flap angles: (a) $M_\infty = 0.25$, $\alpha_w = 0^o$, (b) $Ma = 0.25$, $\alpha_w = 5^o$, (c) $Ma = 0.8$, $\alpha_w = 0^o$, (d) $Ma = 0.8$, $\alpha_w = 5^o$.

Figures 20 through 23 shows the errors in the influence boundary calculations compared to the full domain calculations. The errors in the lift coefficient are defined by the equation below

$$E = 100 * \frac{(C_{L(F.D)} - C_{L(I.B)})}{\left| C_{L(F.D)} \right|_{max}},$$
(6)

where the subscript F.D and I.B respectively indicate full domain or influence boundary calculations and the denominator is the maximum value of all full domain calculations at a given wing angle of attack and Mach number. Similar expressions are used for computing the error in the drag and pitching moment coefficients.

The results show that the errors in the influence boundary calculations increase with the flap angle of attack. In addition, the error in the lift and pitching moment coefficients vary proportionally with the flap angle at the same rate while the error in the drag coefficient varies proportionally with the flap angle at a greater rate. In addition, the relative errors are less at the higher Mach number.

The time taken for the influence boundary calculation relative to the full domain calculations is presented in Fig. 24. The relative time taken varies approximately between 12% for the smallest domain to 38% for the largest domain. The time taken for the influence boundary calculations vary between 20% and 32%.

The results show that the automatically determined influence boundary calculations minimized the errors in the influence boundary calculations without increasing the resource requirements. In addition, calculations with the automatically determined influence boundary domain remove the guesswork from how big or what shape the influence domain needs to be. Figure 25 shows the errors in both the wing and flap aerodynamics based on the automatically determined influence boundary calculations showing the relationship between the error and the Mach number and flap angles. Finally, the present calculations indicate that for the current airfoil/flap configuration, calculations with errors below 20% at $M_\infty = 0.25$ and 10% at $M_\infty = 0.8$ can be obtained at about 30% of the computational requirements of a full domain calculation. The errors are expected to further reduce with the ratio of the flap to airfoil dimensions.
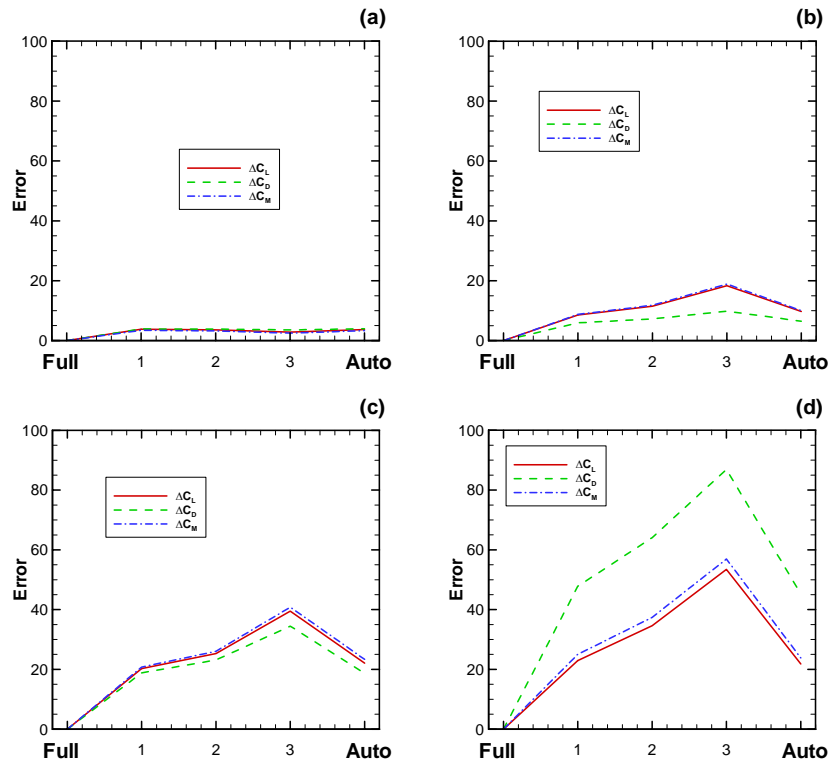
Figure 20. Error in the influence boundary calculations compared to full domain calculations at M_∞=0.25, 0° wing angle of attack (a) α_f=0°, (b) α_f=10°, (c) α_f=20°, and (d) α_f=30°.
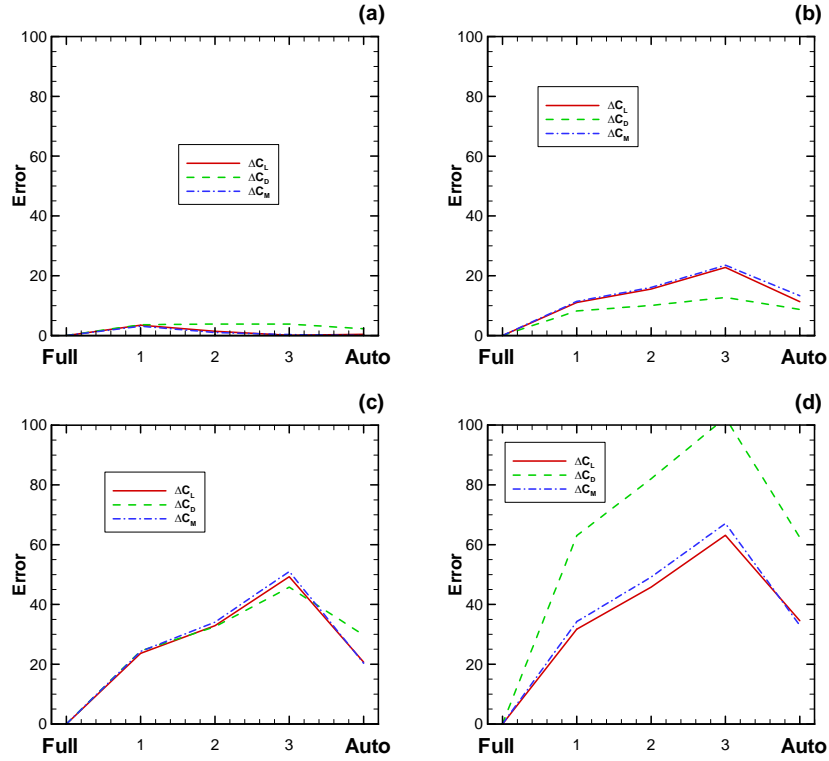
Figure 21. Error in the influence boundary calculations compared to full domain calculations at $M_\infty=0.25$, 5° **wing angle of attack (a)** $\alpha_f=0^o$**, (b)** $\alpha_f=10^o$**, (c)** $\alpha_f=20^o$**, and (d)** $\alpha_f=30^o$**.**
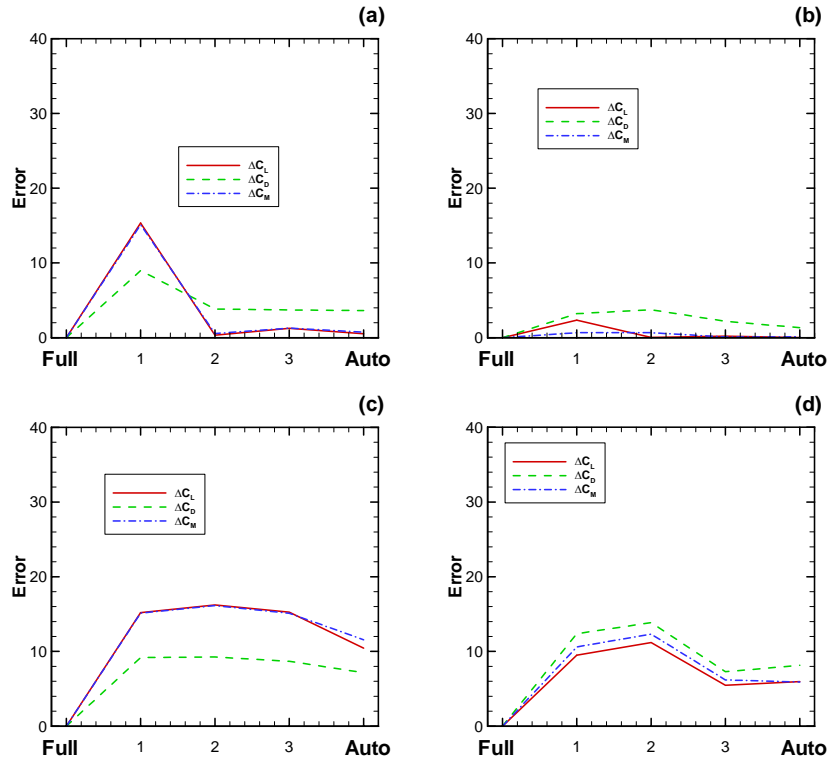
Figure 22. Error in the influence boundary calculations compared to full domain calculations at $M_\infty=0.8$, 0° **wing angle of attack (a)** $\alpha_f=0^o$**, (b)** $\alpha_f=10^o$**, (c)** $\alpha_f=20^o$**, and (d)** $\alpha_f=30^o$**.**

American Institute of Aeronautics and Astronautics
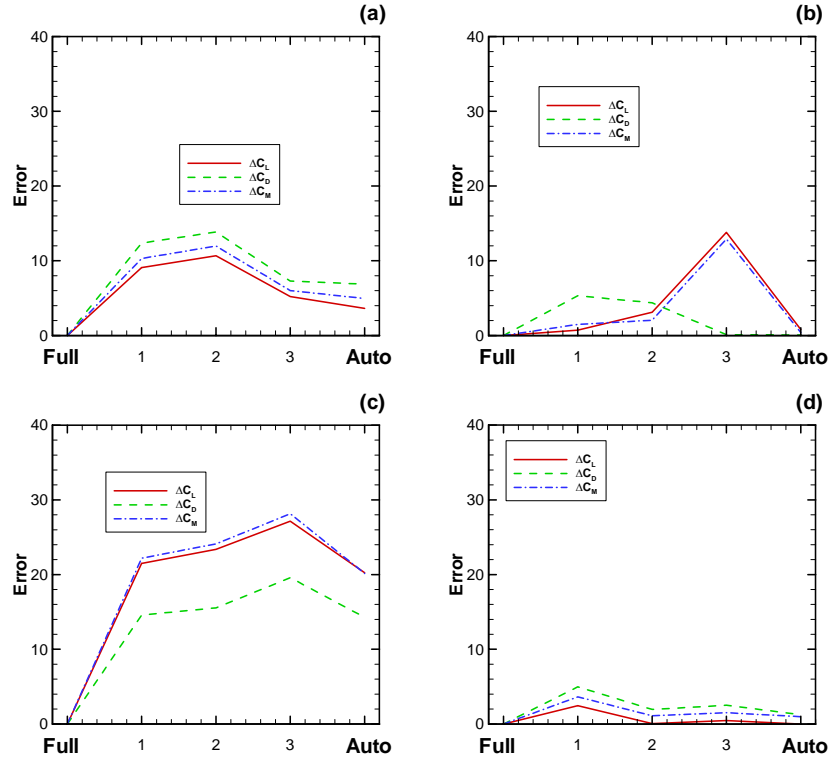
Figure 23. Error in the influence boundary calculations compared to full domain calculations at $M_\infty=0.8$, 5° wing angle of attack (a) $\alpha_f=0^o$, (b) $\alpha_f=10^o$, (c) $\alpha_f=20^o$, and (d) $\alpha_f=30^o$.
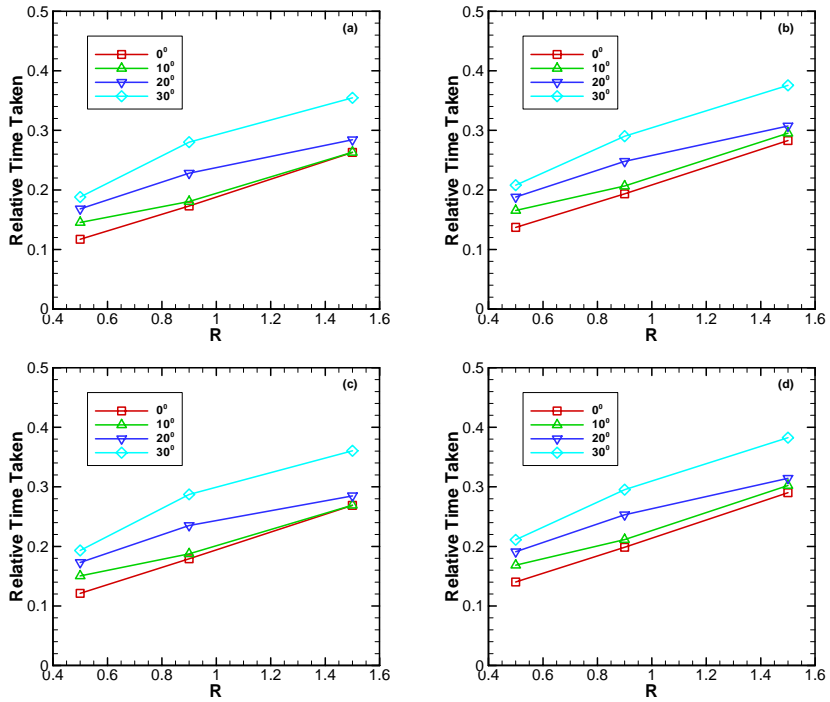
Figure 24. Relative time taken compared to full domain simulations for the influence boundary calculations (a) $M_\infty=0.25$, $\alpha_w=0^o$, (a) $M_\infty=0.25$, $\alpha_w=5^o$, (a) $M_\infty=0.8$, $\alpha_w=0^o$, (a) $M_\infty=0.8$, $\alpha_w=5^o$.
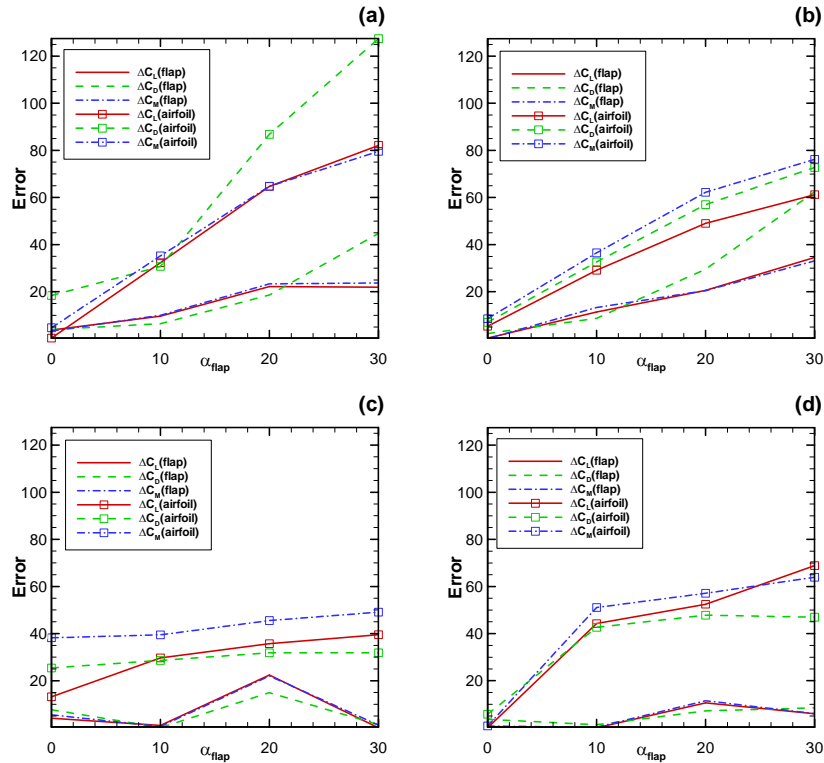
Figure 25. Error in the influence boundary calculations compared to full domain calculations at (a) $M_\infty=0.25$, $\alpha_w=0^o$, (b) $M_\infty=0.25$, $\alpha_w=10^o$, (c) $M_\infty=0.8, \alpha_w=0^o$, and (d) $M_\infty=0.8$, $\alpha_w=5^o$.

2. Wing/Store Configuration

Calculations were done for flow past a wing store combination. The physical domain is illustrated in figure 26. The dimensions in the figure are in inches. The wing has a NACA 0012 profile and is three-dimensional while the store is an ellipsoid.
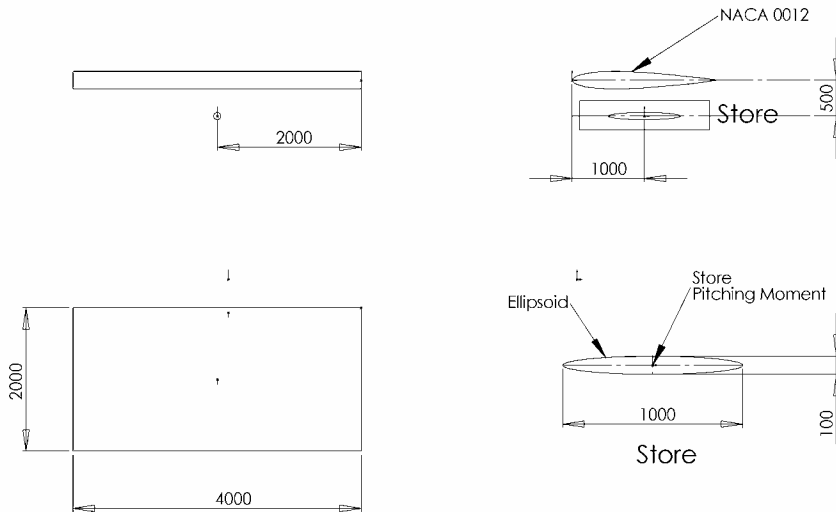
Figure 26. Wing/Store Configuration.

American Institute of Aeronautics and Astronautics

The wing grid uses an O-grid with *249* x *55* x *41* grid points. The store grid is an axisymmetric grid with *51* x *31* x *41* grid points. The grids are shown in Figs. 27 and 28. The grids were generated separately and assembled in the solver using grid transformation procedures to appropriately scale and translate them to the required relative positions. The wing chord length, *C*, is used as the length scale. The overset procedure was used for the full domain calculations to supply boundary values and convey solutions between both grids. Figure 29(a) shows the surface grids after assembly while Fig. 29(b) shows a section through the grids after the overset procedure was completed.

Two types of calculations are performed. In the first type, the flow over the integrated wing and store configuration is calculated. In the second type of calculation, or influence boundary calculations, flow over the store alone is calculated using a small grid surrounding the store. Boundary conditions to this calculation are provided using values from calculations of the wing alone. The differences between both types of calculations are computed.

The influence boundary calculations used four minimized domains of different sizes to determine the effect of the influence boundary domain on the errors. The four influence boundary domains are shown in Fig. 30. Calculations were done at Mach number, $M_\infty = 0.8$ and 1.5, two angles of attack, $\alpha_w = 0^o$ and 5°, and three store separation distances, $S/C = 0.25$, 0.5, and 1.0.The calculations are based on the Euler equations and utilize the WENO scheme for spatial differentiation and Beam-Warming scheme for time integration.

a)   b)
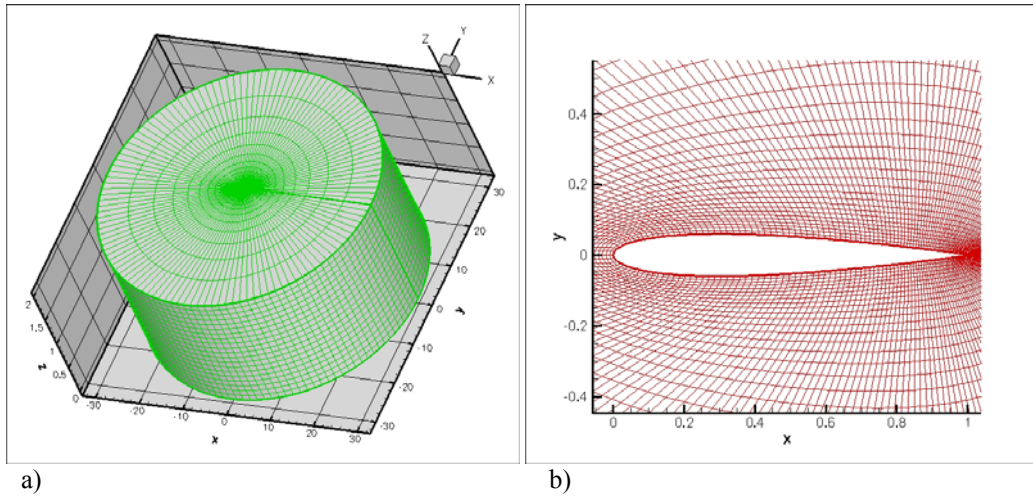
Figure 27. Wing mesh (a) Full grid, (b) Plane section through grid at *Z = 1.0*.

a)   b)
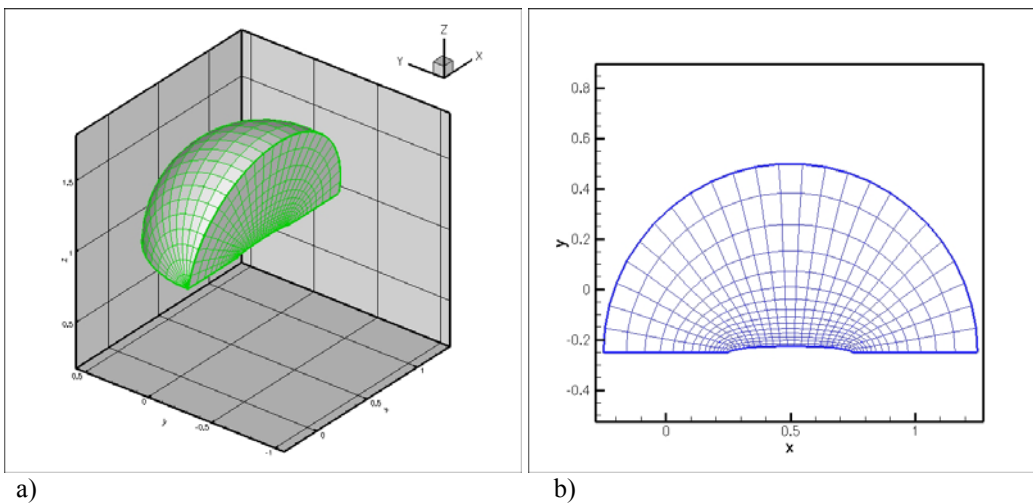
Figure 28. Store mesh with every other grid point removed (a) Section of full grid, (b) Axisymmetric section through grid.
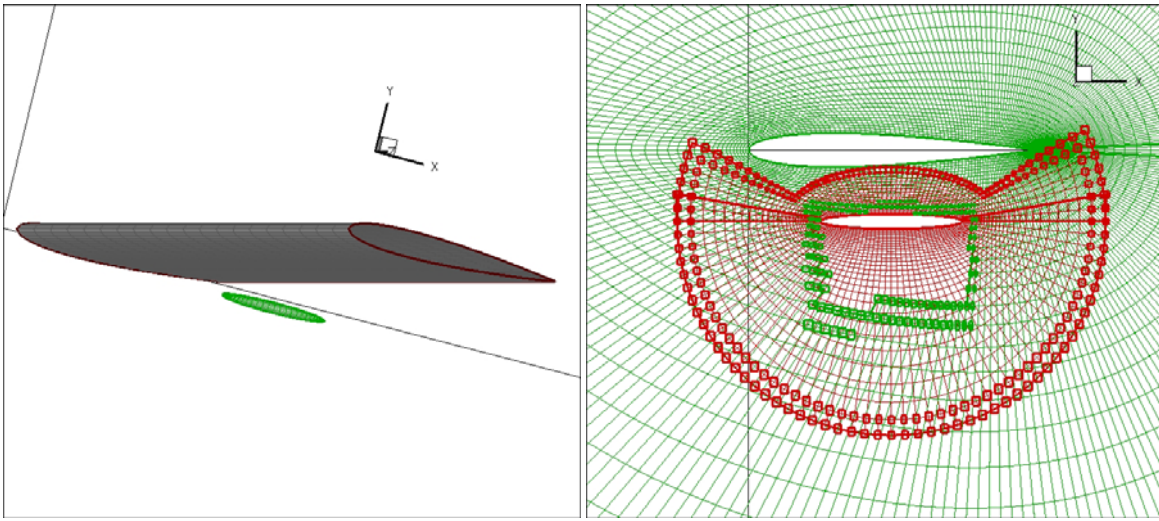
(a)   (b)

Figure 29 Combined grid (a) Surface grid of the wing and the store with every other grid point removed (b) Plane section at *z/C* = 1.0 showing overset nodes of both grids.
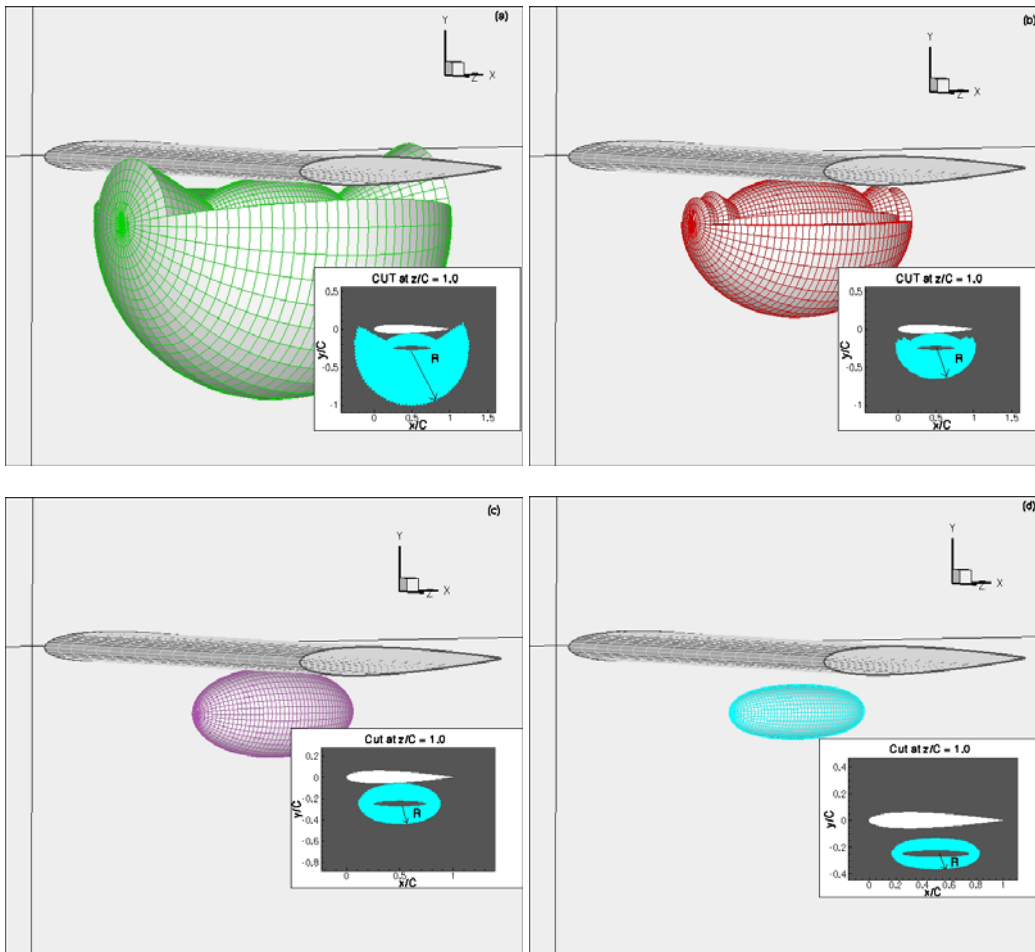
Figure 30 Influence boundary domains (a) Domain 1, *R* ~ 0.75, (b) Domain 2, *R* ~ 0.45, (c) Domain 3, *R* ~ 0.20, (c) Domain 4, R ~ 0.12.

Figures 31 though 34 shows the lift coefficient, C_L, for the calculations while Figs. 35 though 38 show the drag coefficient, C_D, for the calculations. Focusing on the store aerodynamic quantities, the figures show that the errors in the influence boundary calculations vary with the influence boundary size. In fact, it can be observed that there is an optimum influence domain size at which the error is a minimum. Table 1 through 4 shows the error in the influence boundary calculations. The errors vary averagely from 5% to 28% at $Ma = 0.8$ and 2% to 20% at $Ma = 1.5$ for the lift coefficient and 20% to 40% at $M_\infty = 0.8$ and 2% to 12% at $M_\infty = 1.5$ for the drag coefficient. The large values are due to the small values of the denominator in Eq. (6). The errors are reduced at the higher Mach number.

The time taken for the influence boundary calculation relative to the full domain calculations is presented in Fig. 39. The relative time taken varies approximately between 16% for the smallest to 24% for the largest domain.
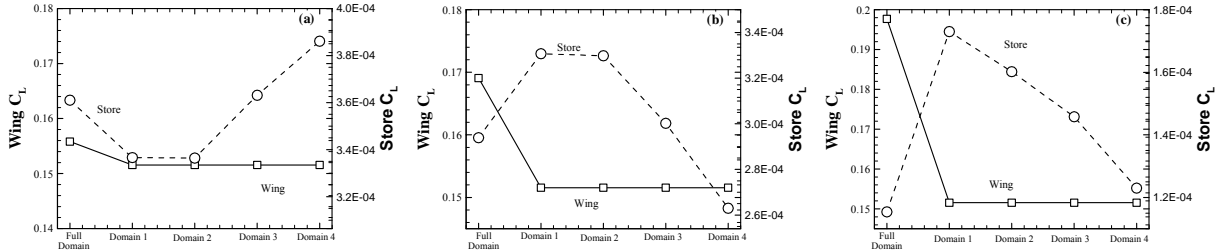
Figure 31. Lift coefficient variation due to the size of the influence boundary domain for $M_\infty=0.8$, $\alpha_w=0^o$ and store separation distance: (a) $S/C = 0.25$, (b) $S/C = 0.5$, (c) $S/C = 1.0$.
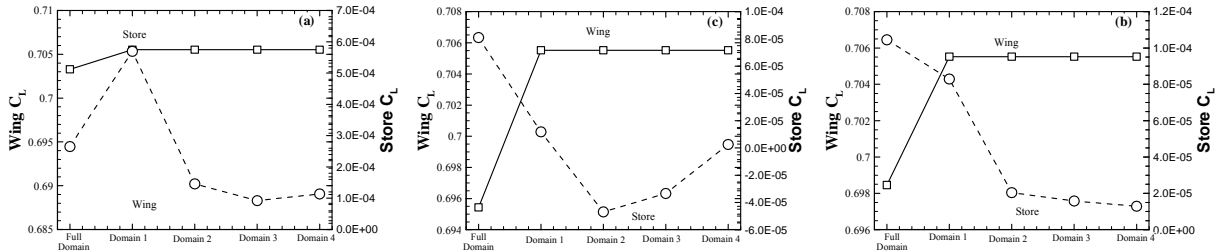
Figure 32. Lift coefficient variation due to the size of the influence boundary domain for $M_\infty=0.8$, $\alpha_w=5^o$ and store separation distance: (a) $S/C = 0.25$, (b) $S/C = 0.5$, (c) $S/C = 1.0$.
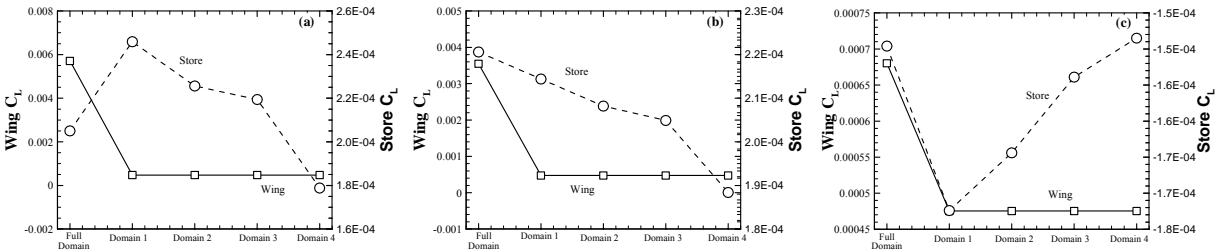
Figure 33. Lift coefficient variation due to the size of the influence boundary domain for $M_\infty=1.5$, $\alpha_w=0^o$ and store separation distance: (a) $S/C = 0.25$, (b) $S/C = 0.5$, (c) $S/C = 1.0$.
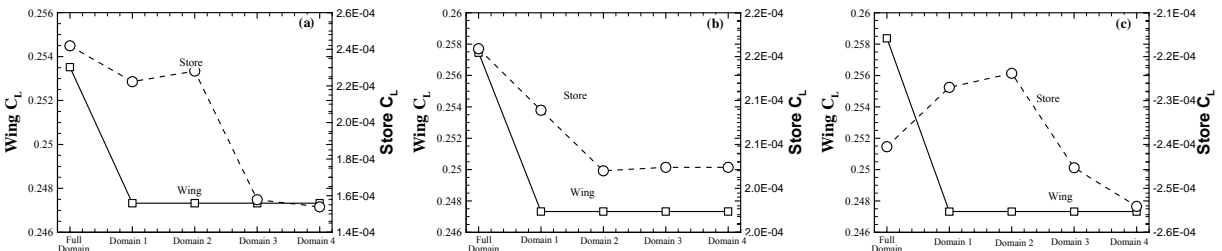
Figure 34. Lift coefficient variation due to the size of the influence boundary domain for $M_\infty=1.5$, $\alpha_w=5^o$ and store separation distance: (a) $S/C = 0.25$, (b) $S/C = 0.5$, (c) $S/C = 1.0$.
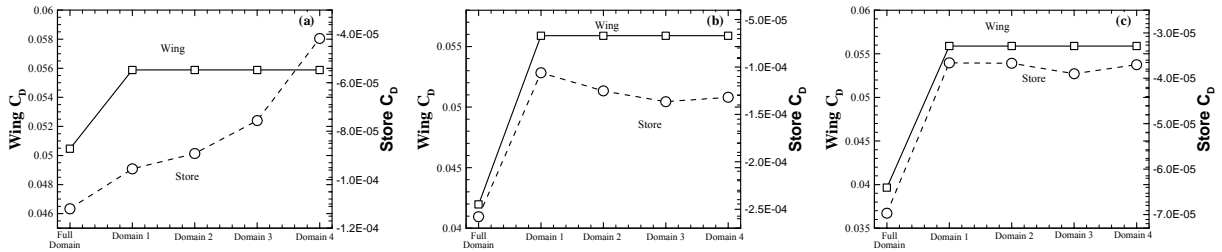
Figure 35. Drag coefficient variation due to the size of the influence boundary domain for $M_\infty=0.8$, $\alpha_w=0^o$ and store separation distance: (a) $S/C = 0.25$, (b) $S/C = 0.5$, (c) $S/C = 1.0$.
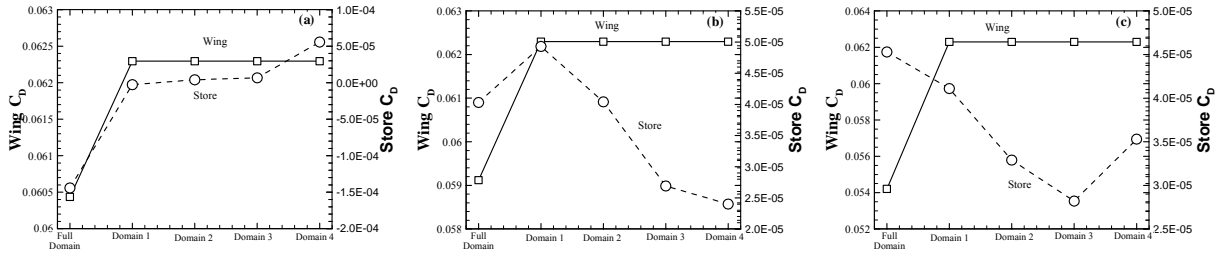
Figure 36. Drag coefficient variation due to the size of the influence boundary domain for $M_\infty=0.8$, $\alpha_w=5^o$ and store separation distance: (a) $S/C = 0.25$, (b) $S/C = 0.5$, (c) $S/C = 1.0$.
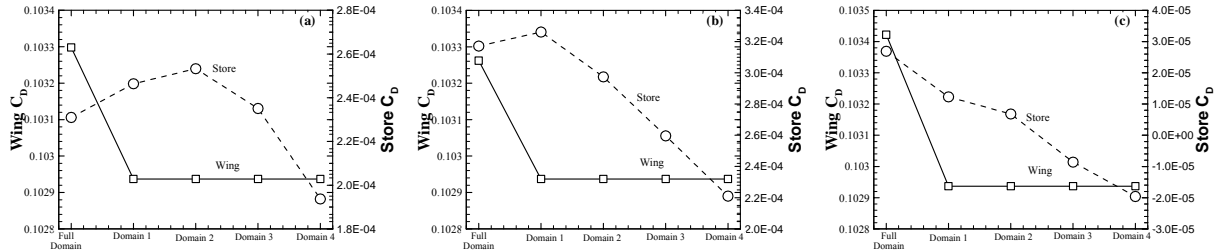
Figure 37. Drag coefficient variation due to the size of the influence boundary domain for $M_\infty=1.5$, $\alpha_w=0^o$ and store separation distance: (a) $S/C = 0.25$, (b) $S/C = 0.5$, (c) $S/C = 1.0$.
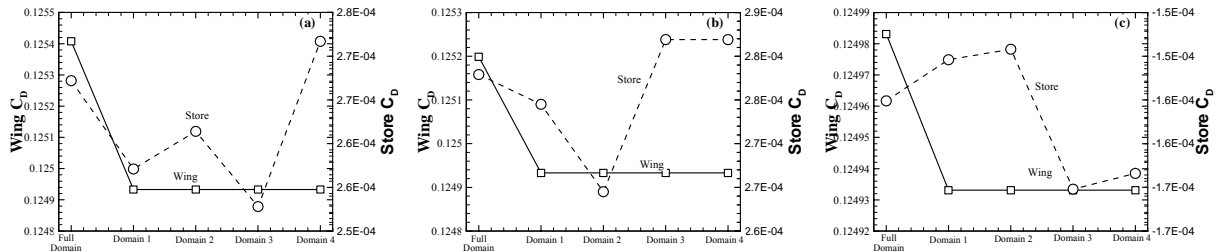
Figure 38. Drag coefficient variation due to the size of the influence boundary domain for $M_\infty=1.5$, $\alpha_w=5^o$ and store separation distance: (a) $S/C = 0.25$, (b) $S/C = 0.5$, (c) $S/C = 1.0$.

Table 3. Relative errors for influence boundary calculations for $\alpha_w = 0^o$, $M_\infty = 0.8$.

			% Errors					
			S/C = 0.25		S/C = 0.50		S/C = 1.0	
	Domain	R	C_L	C_D	C_L	C_D	C_L	C_D
Flap	1	0.75	6.8	6.4	10.2	58.9	16.0	12.8
	2	0.45	6.8	8.8	9.9	51.5	12.4	12.8
	3	0.20	0.6	14.1	1.7	47.0	8.4	11.9
	4	0.12	7.0	27.3	8.6	48.9	2.1	12.7
Wing			2.2	10.7	8.9	27.6	23.3	32.2

Table 4. Relative errors for influence boundary calculations for $\alpha_w = 5^o$, $M_\infty = 0.8$.

			% Errors					
			S/C = 0.25		S/C = 0.50		S/C = 1.0	
	Domain	R	C_L	C_D	C_L	C_D	C_L	C_D
Flap	1	0.75	114.8	98.1	8.1	6.2	26.1	10.4
	2	0.45	45.0	102.8	31.7	0.1	48.2	30.8
	3	0.20	65.1	104.6	33.5	9.3	43.2	42.4
	4	0.12	57.1	138.6	34.6	11.3	29.6	24.8
Wing			0.3	3.1	1.0	5.3	1.4	13.4

Table 5. Relative errors for influence boundary calculations for $\alpha_w = 0^o$, $M_\infty = 1.5$.

			% Errors					
			S/C = 0.25		S/C = 0.50		S/C = 1.0	
	Domain	R	C_L	C_D	C_L	C_D	C_L	C_D
Flap	1	0.75	18.5	4.9	2.8	2.8	10.3	4.6
	2	0.45	9.3	7.0	5.6	6.2	6.7	6.3
	3	0.20	6.5	1.3	7.1	18.1	1.9	11.2
	4	0.12	11.9	11.8	14.6	30.3	0.5	14.7
Wing			91.7	0.3	53.8	0.3	3.6	0.5

Table 4. Relative errors for influence boundary calculations for $\alpha_w = 5^o$, $M_\infty = 1.5$.

			% Errors					
			S/C = 0.25		S/C = 0.50		S/C = 1.0	
	Domain	R	C_L	C_D	C_L	C_D	C_L	C_D
Flap	1	0.75	8.1	3.6	2.9	1.2	5.6	1.7
	2	0.45	5.7	2.1	5.7	4.8	6.9	2.1
	3	0.20	34.8	5.2	5.6	1.4	2.0	3.6
	4	0.12	36.4	1.6	5.6	1.4	5.6	3.0
Wing			2.4	0.4	3.9	0.2	4.3	0.0

American Institute of Aeronautics and Astronautics
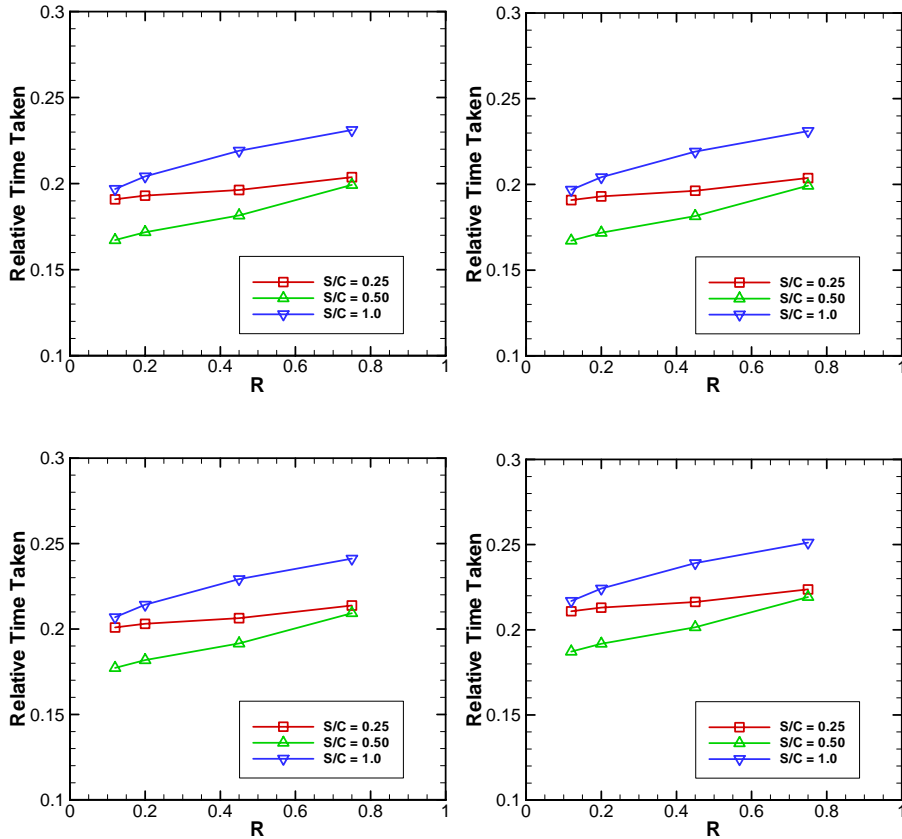
Figure 39. Relative time taken compared to full domain simulations for the influence boundary calculations:, (a) $M_\infty=0.8$ $\alpha_w=0^o$, (b) $M_\infty=0.8$ $\alpha_w=5^o$, (c) $M_\infty=1.5$ $\alpha_w=0^o$, (d) $M_\infty=1.5$ $\alpha_w=5^o$).

IV.   Conclusion

The current paper presents procedures for influence boundary calculations, which are based on reducing the scope and resource requirements of a computational fluid dynamics problem while minimizing the error in the approximated domain by a systematic application of the effects of the full or surrounding domain on the reduced domain.

Equations and automatic procedures for determining the reduced domain are presented. The procedure is validated using flow over a cylinder, airfoil, and B747-200 aircraft. The error in the procedure is determined for an airfoil/flap and wing/store configuration. The results show that the automatically determined influence domain procedure obviates the need for ad-hoc determination of the size and shape of the influence domain while minimizing the error in the influence boundary calculation. In addition, it was demonstrated that calculations with errors below 20% at $M_\infty = 0.25$ and 10% at $M_\infty = 0.8$ can be obtained at about 30% of the computational cost of a full domain calculation.

References

[1]Davis, M.B., Welterlen, T.J, and Corfeld, K.J. 2003. "Minimized Domain CFD for Store Separation". AIAA Paper 2003-1245.

[2]Cenko, A., Meyer, R., and Tessitore, F. 1986. "Further Development of the Influence Function Method for Store Aerodynamic Analysis.", J. Aircraft, 23, 8.

[3]Alabi, K. & Ladeinde, F., 2004. "Parallel, high-order overset grid implementation for supersonic flows". AIAA Paper 2004-1178.

[4]Alabi, K. & Ladeinde, F., 2005. "Treatment of Hole Nodes in a High-Order Overset Procedure for Supersonic Flows". AIAA Paper 2005-0437.

[5]Rogers S.E., Roth, K., Nash, S.M., Baker, D.M., Slotnick J.P., Whitlock M., Cao H.V. "Advances In Overset CFD Processes Applied to Subsonic High-Lift Aircraft.", AIAA Paper 2000-4216, AIAA Applied Aerodynamics Conference, 2000, Denver Co.

[6]Snyder, R.D. and Scott, J.N., "An Overset Grid Solver with Method Coupling and Feature Tracking," AIAA Paper 99-3290, 1999.

[7]Josyula, E and Gordnier, R.E., " Computational Simulation of the F-22 Aircraft," AIAA Paper 98-0526, 36th Aerospace Sciences Meeting, Reno, NV, January 1998.

[8]Lee, Y. and Baeder, J.D., "High-Order Overset Method for Blade Vortex Interaction," AIAA Paper 02-0559, AIAA 40th Aerospace Sciences Meeting Reno, NV, January 2002.

[9]Sherer, S.E & Scott, J.N., 2002. Development and Validation of a High Order Overset Grid Flow Solver". AIAA Paper 2002-2733.

[10]Murman, S., Chaderjian, N, & Shishir, P., "Automation of a Navier-Stokes S&C Database Generation for the Harrier in Ground Effect". AIAA Paper 2002-0259, 2002.

[11]Noack, R,, "Resolution Appropriate Overset Grid Assembly for Structured and Unstructured Grids". AIAA Paper 2003-4123, 2003.

[12]Rogers S., Suhs, N., Dietz, W., Nash, S., Onufer, J., "PEGASUS User's Guide ", 2003.

[13]Nakahashi, K., Togashi, F., & Sharov, D., "Intergrid-Boundary Definition Method for Overset Unstructured Grid Approach," AIAA Journal, 38, 11. 2000.

[14]Thaerocomp Technical Corp., "AEROFLO Sample Problems Manuals," 2005.

[15]Visbal, M.R. and Gaitonde, D.V., "High-Order-Accurate Methods for Complex Unsteady Subsonic Flows," AIAA Journal, Vol. 37, No. 10, 1999, pp. 1231-1239.

[16]Jiang, G. -S. and Shu, C. -W. "Efficient Implementation of Weighted ENO Schemes", J. Comput. Phys., Vol 126, 202, 1996.

[17]Ladeinde, F., Alabi, K., Safta, C., Cai, X., 2006. "The First High –Order Simulation of Aircraft: Challenges and Opportunities", AIAA 2006-1526. 44th Aerospace Sciences Meeting, Reno, NV, January 2006.

American Institute of Aeronautics and Astronautics